Supporting Information

Difference in reaction mechanism between $ZnZrO_x$ and $InZrO_x$ for CO_2 hydrogenation

Shohei Tada [1,*], Yurika Ogura [2], Motohiro Sato [3], Akihiro Yoshida [3,4], Tetsuo Honma 5, Masahiko Nishijima [6], Tatsuya Joutsuka [7*], Ryuji Kikuchi [1,*]

1 Division of Applied Chemistry, Graduate School of Engineering, Hokkaido University, Sapporo, Hokkaido 060-8628, Japan
2 Department of Materials Science and Engineering, Ibaraki University, 4-12-1, Nakanarusawa, Hitachi, Ibaraki 316-851, Japan
3 Graduate School of Science and Technology, Hirosaki University, 3 Bunkyo-cho, Hirosaki, Aomori 030-8651, Japan
4 Institute of Regional Innovation, Hirosaki University, 3 Bunkyo-cho, Hirosaki, Aomori 030-8651, Japan
5 Japan Synchrotron Radiation Research Institute, Sayo-gun, Hyogo 679-5198, Japan
6 Flexible 3D System Integration Laboratory, Osaka University, 8-1 Mihogaoka Ibaraki-shi, Osaka 567-0047, Japan.
7 Department of Materials Science and Engineering, Ehime University, 3 Bunkyo-cho, Matsuyama, Ehime 790-8577, Japan

Corresponding authors:
Shohei Tada (shohei.tada.st@eng.hokudai.ac.jp)
Tatsuya Joutsuka (joutsuka.tatsuya.zk@ehime-u.ac.jp)
Ryuji Kikuchi (rkikuchi8@eng.hokudai.ac.jp)

Detail procedure

X-ray fluorescence (XRF). We used a Malvern Panalytical Epsilon 1 instrument with Ag radiation to analyze the catalyst composition. Omnian software (Malvern Panalytical) was used to analyze the raw data.

X-ray diffraction (XRD). We used a Rigaku Ultima IV with Cu-Kα radiation to conduct XRD measurements. The voltage and current were set at 40 kV and 20 mA, respectively.

N_2 adsorption and desorption. We conducted N_2 adsorption and desorption measurements using a MicrotracBEL BELSORP-MINI-II instrument to analyze the specific surface areas and pore volumes of the samples. Approximately 0.1 g of the sample was heated at 150 °C for 2 h under vacuum (MicrotracBEL BELPREP VAC-II) prior to measurement. N_2 adsorption and desorption were performed at liquid nitrogen temperature (−196 °C). The specific surface area was determined from the results obtained using the Brunauer-Emmett-Teller method. The total pore volume was calculated to be $p/p_0 = 0.98$.

X-ray absorption (XAS). The Zn K-edge and In K-edge XAS spectra of the samples were obtained using the BL14B2 beamline at SPring-8 according to the procedure described in our previous report. [1] The samples were mixed with BN and pressed into thin disks (10 mm I.D.). The spectra were corrected and normalized using the Athena and Artemis software. [2] The radial structure function (RSF) was obtained by the Fourier transformation of the k^3-weighted experimental $\chi(k)$ function in the R space. The theoretical phase shift and amplitude functions were calculated using the FEFF6 program.

Scanning transmission electron microscopy (STEM). STEM was used to observe the catalyst powder directly (JEOL, JEM-ARM200F). The samples were then dispersed in ethanol, dropped onto Cu microgrids (Ohkenshoji, NP-C15) and dried. Elemental maps of Zn, In, and Zr were obtained using energy-dispersive X-ray spectroscopy.

Accuracy of computational setup

We here discuss the accuracy of our computational setup. To check the effect of the thickness of our slab model, we prepared a larger slab with the number of ZrO_2 layers of four, yielding 144 atoms in the neat ZrO_2 slab. The same positions of In and oxygen vacancy as in the case of two-ZrO_2-layer model yielded the *t*-$InZrO_x$ (101) surface shown in **Figure S9**. The thickness of the vacuum region along the surface normal direction is 15 Å, which is the same as the two-layer model. During the geometry optimization, the coordinates of the atoms, except for the two bottom layers, were optimized to follow the previous computational study.[3] The other computational conditions were the same for both two-layer and four-layer models. We first optimized the geometry of the four-layer ZrO_2 slab and put the adsorbates on the optimized slab using the geometries employed to calculate the energy profile in **Figure 5**. We here discuss the activation free energies in the rate-limiting step of each reaction pathway and the free energies of the reactants and products.

Figure S10 and **Figure S11** respectively show the structures of the reaction intermediates and transition states (TSs) using the four-layer model, and **Tables S2** and **S3** respectively summarizes the results of computed free energy of the intermediates and activation free energies. The free energies of the intermediates change randomly due to the larger electronic and structural relaxation arising from larger number of atoms. The activation free energy changes much smaller than the free energies of the intermediates. The order of activation free energy in each pathway holds (CO pathway < formate pathway < methane pathway), and therefore the two-layer model is shown to be a fine approximation to the four-layer model to discuss of reaction mechanism by DFT calculations.

Free-energy calculations. The free energies of the adsorbates or transition states at temperature T were computed using the normal mode analysis. The Gibbs free energy for gas-phase molecules was calculated by $G = E_{\mathrm{e}} + E_{\mathrm{trans}} + E_{\mathrm{rot}} + E_{\mathrm{vib}} - T(S_{\mathrm{trans}} + S_{\mathrm{rot}} + S_{\mathrm{vib}})$ (S: entropy), while that for adsorbed molecules on the surfaces was calculated by $G = E_{\mathrm{e}} + E_{\mathrm{vib}} - TE_{\mathrm{vib}}$. Here, E_{e} is the electronic energy by DFT calculations, the subscript of trans, rot, and vib indicates the translational, rotational, and vibrational contributions, respectively. In addition, $E_{\mathrm{trans}} = 3RT/2$, and

$E_{\text{rot}} = RT$ (for linear molecule) or $3RT/2$ (for non - linear molecule). The vibrational energy and entropy were evaluated using the following equations:

$$E_{\text{vib}} = k_B \sum_i^N \frac{\epsilon_i}{k_B} \left[\frac{1}{2} + \frac{1}{\exp\left(\frac{\epsilon_i}{k_B T}\right) - 1} \right],$$

$$S_{\text{vib}} = k_B \sum_i^N \left[\frac{\epsilon_i}{k_B T \left\{ \exp\left(\frac{\epsilon_i}{k_B T}\right) - 1 \right\}} - \ln\left\{ 1 - \exp\left(-\frac{\epsilon_i}{k_B T} \right) \right\} \right].$$

Here, k_{B} is the Boltzmann constant, and N is the degrees of freedom, and ϵ_i is vibrational energies of ith normal mode. The rotational entropy was evaluated by Gaussian 16 [4] using the configurations of gas-phase molecules optimized with VASP. The temperature was set to 300°C and the pressure was 1.0 MPa.

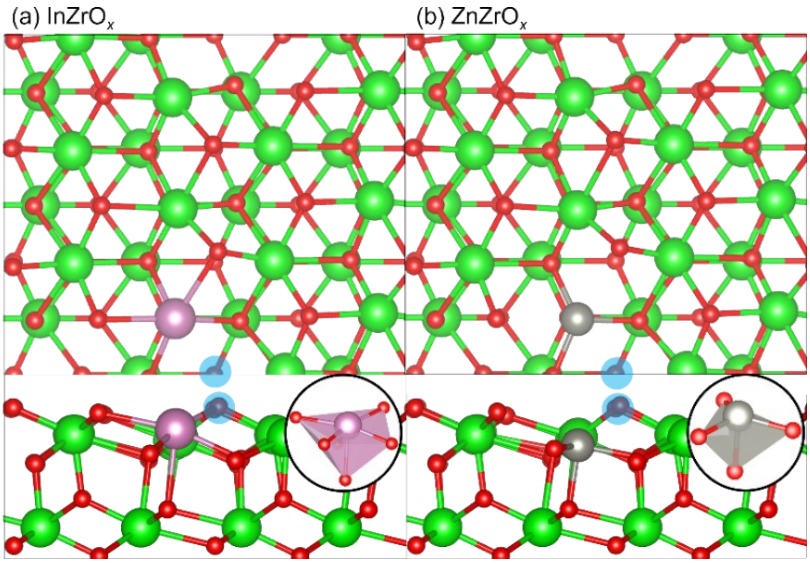

Figure S1 Top and side views of optimized (a) $InZrO_x$ and (b) $ZnZrO_x$ surfaces. The positions of oxygen vacancies are indicated by blue circles. Color code: green: Zr, red: O, purple: In, and gray: Zn. The figures are prepared using VESTA.[5] [InO_6] and [ZnO_4] clusters are shown. The [InO_6] cluster consists of three short In–O bonds with bond lengths $d_{In\text{-}O}$ = 2.20−2.29 Å and three long In–O bonds with $d_{In\text{-}O}$ = 2.51−2.64 Å. The [ZnO_4] cluster consists of four Zn–O bonds with $d_{Zn\text{-}O}$ = 2.00−2.09 Å.

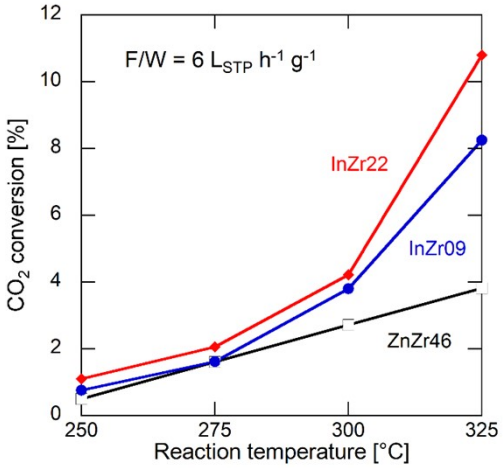

Figure S2 CO_2 conversion over ZnZr46, InZr09, and InZr22 for CO_2 hydrogenation. F/W = 6 L_{STP} h^{-1} g^{-1}. Pressure = 1.0 MPa. Gas composition: $CO_2/H_2/N_2$ = 1/3/1.

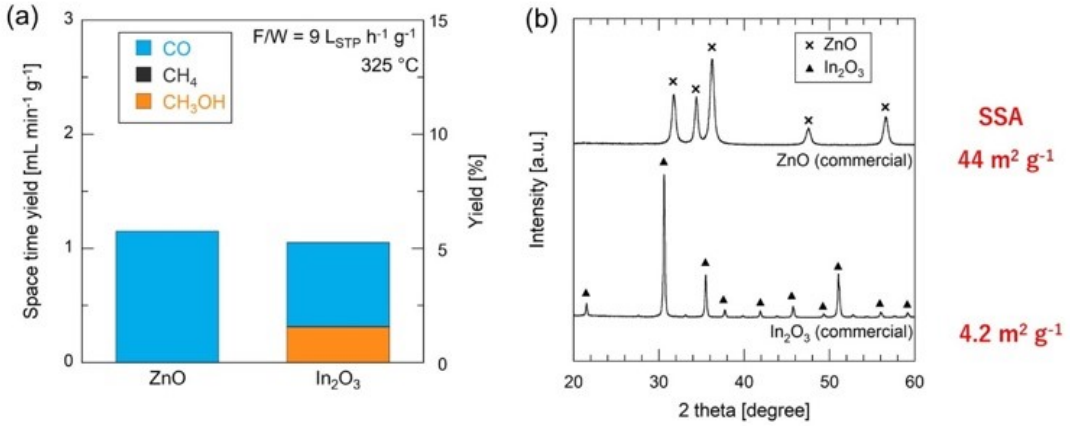

Figure S3 (a) Space time yields and yields of CH_3OH, CO, and CH_4 over In_2O_3 and InZr09, and InZr22 for CO_2 hydrogenation. F/W = 9 L_{STP} h^{-1} g^{-1}. Temperature = 325 °C. Pressure = 1.0 MPa. Gas composition: $CO_2/H_2/N_2$ = 1/3/1. (b) X-ray diffraction (XRD) patterns and specific surface areas of ZnO and In_2O_3.

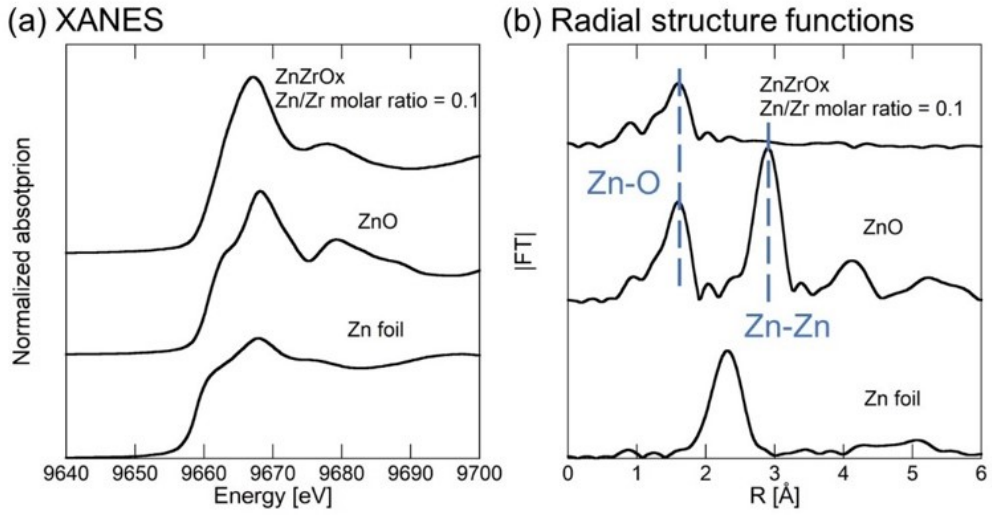

Figure S4 Zn K-edge (a) XANES spectra and (b) Fourier transforms of the k^3-weighted extended XAS fine structure oscillations of Zn foil, ZnO, and $ZnZrO_x$ at Zn/Zr molar ratio = 0.1. k range: 30–140 nm^{-1}.

Figure S4a shows the Zn K-edge X-ray absorption near edge structure (XANES) spectra of Zn foil, ZnO, and $ZnZrO_x$ at a Zn/Zr molar ratio of 0.1. The ZnO spectrum exhibits a strong peak at 9669 eV, corresponding to the transition from Zn 1*s* to Zn 4*p*−O 2*p* hybridized states in the conduction band. [6] A shoulder at 9663 eV is associated with the transition from Zn 1s to Zn 4*sp*−O 2*p* hybridized states. [6] Notably, the $ZnZrO_x$ spectrum closely resembles that of ZnO because of the pronounced peak at 9669 eV. **Figure S4b** shows the Zn K-edge radial structure functions (RSFs). The RSFs exhibit a peak at 1.8 Å, corresponding to the first-nearest neighbor Zn−O distance (1.9−2.0 Å). [7] In contrast, the ZnO RSF displays a peak at 2.9 Å (the first- and second-nearest neighbors Zn−Zn distances of the zinc oxides), [7] whereas the $ZnZrO_x$ RSF does not. Consequently, the Zn^{2+} species in $ZnZrO_x$ exist as isolated [ZnO_a] clusters. [1]

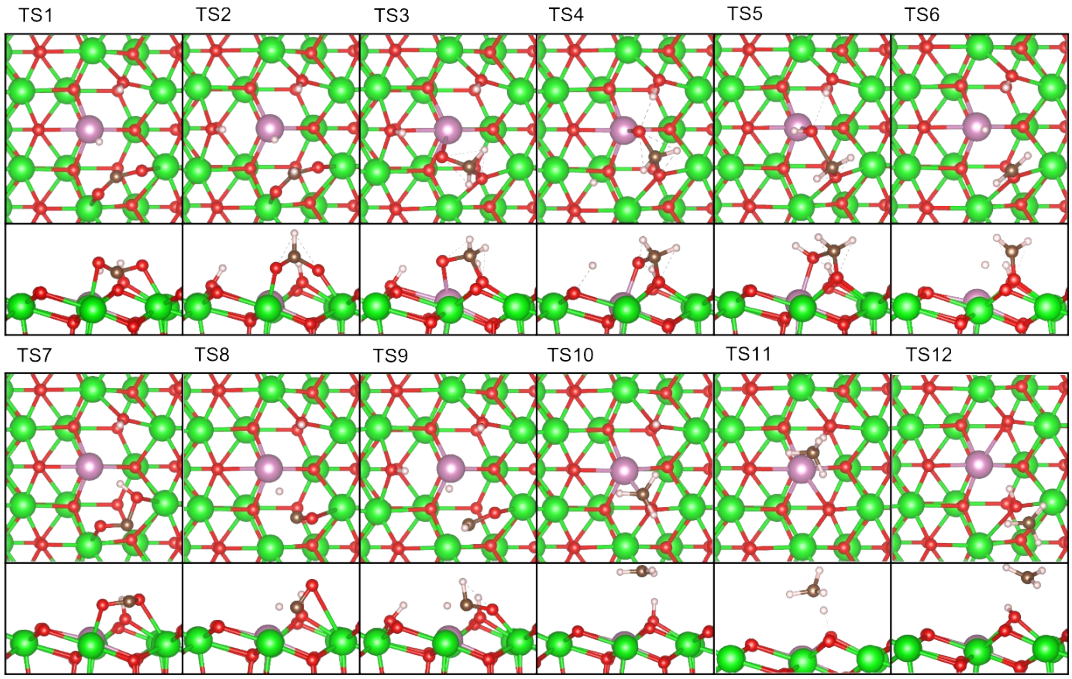

Figure S5 Structures of the transition states in **Figure 5**. Color code: green: Zr, red: O, purple: In, white: H, and brown: C. The figures are prepared using VESTA.

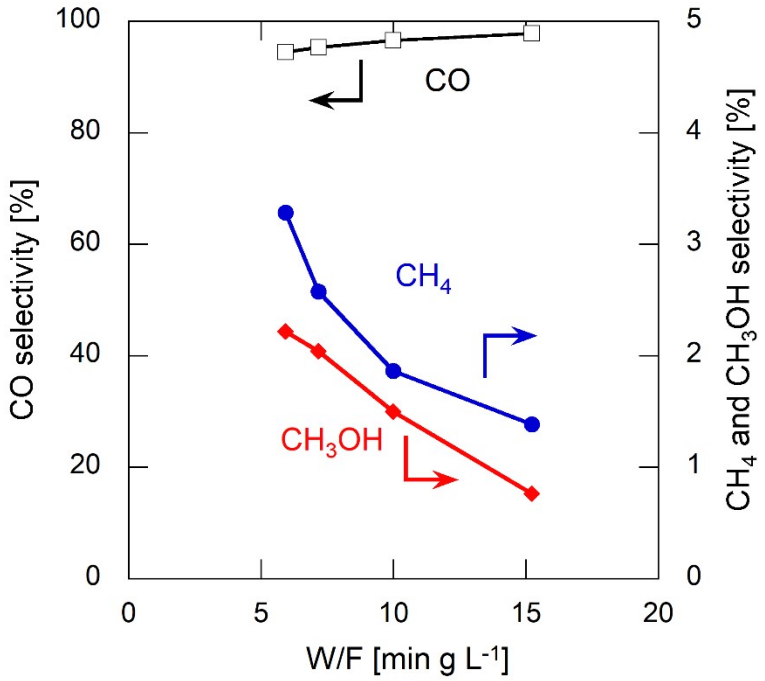

Figure S6 CO, CH_4, and CH_3OH selectivities plotted against contact time (W/F) over InZr09. Reaction gas: $CO_2/H_2/N_2$ = 1/3/1. Pressure = 1.0 MPa. Temperature = 325 °C.

As the contact time (W/F) increases, CO_2 conversion also increases (not shown). Concurrently, CH_3OH selectivity decreases, while CO selectivity increases. This observation suggests that CO_2 hydrogenation over InZr09 follows a stepwise pathway, proceeding from CO_2 through CH_3OH to CO. The high CO selectivity observed at longer contact times indicates that the rate of CH_3OH decomposition to CO is much faster than the rate of CO_2-to-CH_3OH hydrogenation. Interestingly, CH_4 selectivity also decreases with increasing contact time. Based on the results of the CH_3OH conversion reaction tests shown in **Figure 9**, it can be inferred that CH_4 is produced from CH_3OH. If the rate of CH_3OH-to-CH_4 reaction is significantly slower than that of CH_3OH-to-CO reaction (referred to as CH_3OH decomposition to CO), the selectivity trend observed in **Figure S6** can be explained.

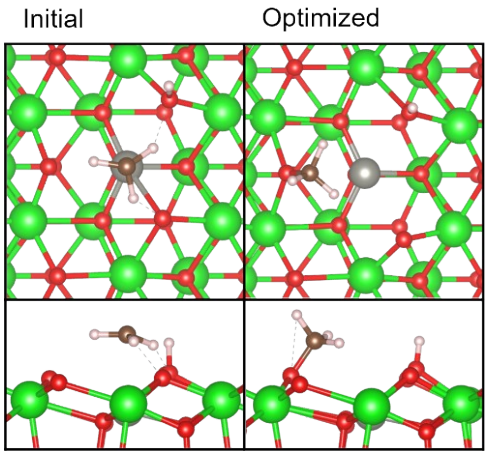

Figure S7 Initial structure for geometry optimization of a methyl group adsorbed on the $ZnZrO_x$ surface and the optimized structure by DFT calculations. Notably, the methyl group in the initial structure transforms into a methoxy group after geometry optimization. Color code: green: Zr, red: O, purple: In, white: H, and brown: C. The figures are made by VESTA. [5]

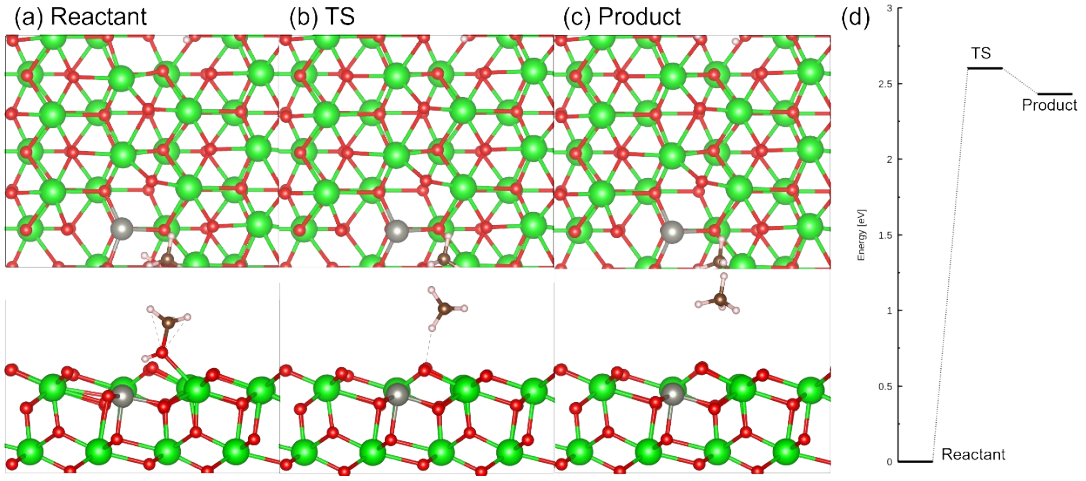

Figure S8 Top and side views of the (a) reactant, (b) TS, and (c) product, and the free energy profile of CH_4 formation by CH_3OH decomposition on the $ZnZrO_x$ surface. The activation free energy is 2.60 eV. Color code: green: Zr, red: O, purple: In, white: H, and brown: C. The figures are made by VESTA. [5]

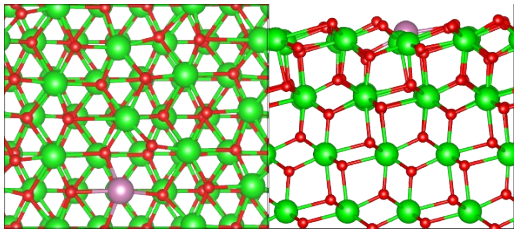

Figure S9 Four-layer model of *t*-$InZrO_x$ (101) surface.

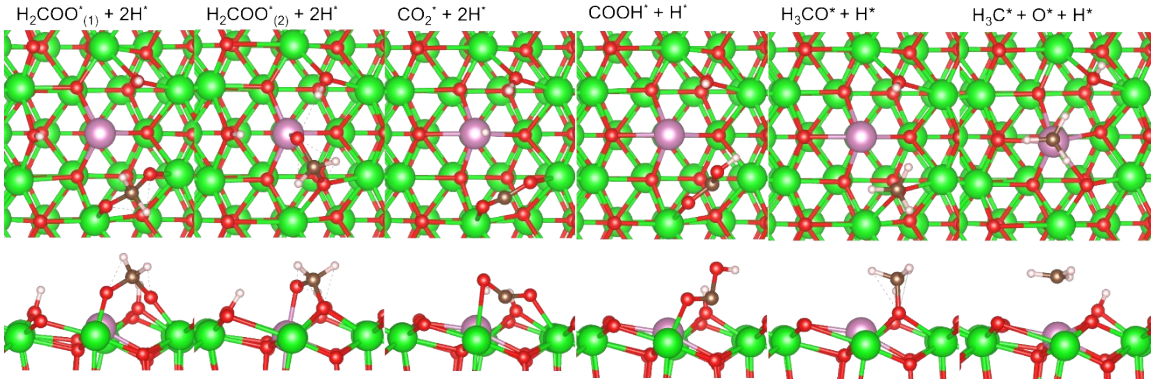

Figure S10 The structures of reaction intermediates using the four-layer model.

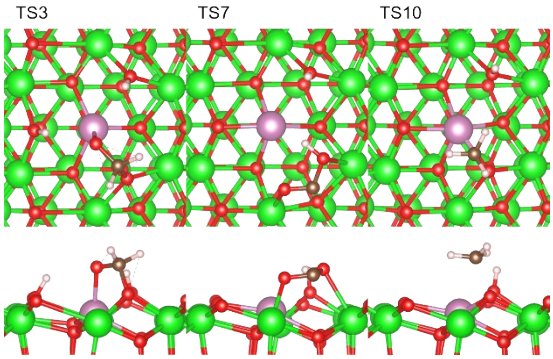

Figure S11 The structures of TSs using the four-layer model.

Table S1 Adsorption energies (E_{ads}) in eV for the reactants, intermediates, and products in **Figure 5**. In these calculations, the initial coordinates of each molecule were extracted from the coordinates in the calculations of **Figure 5**, and the geometry of each molecule was optimized.

	CO_2	H_2	HCOO	CO	H_2CO	H_2CO	H_2COOH	HCO	H_2O	H_3COH
E_{ads}	−0.76	0.02	−5.01	−0.69	−1.33	−5.14	−4.73	−2.89	−0.30	−1.02

Table S2 Free energies (in eV) of the key reaction intermediates in **Figure 5** using two- and four-layer models.

Number of layers	H_2COOH^* (1) + $2H^*$	H_2COOH^* (2) + $2H^*$	CO_2 + $2H^*$	$COOH^*$ + H^*	H_3CO^* + H^*	H_3C^* + O^* + H^*
2	−0.51	+0.59	+0.50	+0.36	−0.59	+0.28
4	−0.38	+1.03	+0.78	+0.64	−0.32	+0.54

Table S3 Activation free energies (in eV) of TS3, TS8, and TS11 (key steps in CO_2 hydrogenation to methanol) using two- and four-layer models.

Number of layers	TS3	TS7	TS11
2	1.28	1.02	1.52
4	1.39	1.00	1.65

References

1. S. Tada, N. Ochiai, H. Kinoshita, M. Yoshida, N. Shimada, T. Joutsuka, M. Nishijima, T. Honma, N. Yamauchi, Y. Kobayashi and K. Iyoki, *ACS Catal.*, 2022, **12**, 7748-7759.
2. B. Ravel and M. Newville, *J. Synchrotron Rad.*, 2005, **12**, 537-541.
3. J. J. Wang, G. N. Li, Z. L. Li, C. Z. Tang, Z. C. Feng, H. Y. An, H. L. Liu, T. F. Liu and C. Li, *Sci. Adv.*, 2017, **3**, e170129.
4. M. J. Frisch, G. W. Trucks, H. B. Schlegel, G. E. Scuseria, M. A. Robb, J. R. Cheeseman, G. Scalmani, V. Barone, G. A. Petersson, H. Nakatsuji, X. Li, M. Caricato, A. V. Marenich, J. Bloino, B. G. Janesko, R. Gomperts, B. Mennucci, H. P. Hratchian, J. V. Ortiz, A. F. Izmaylov, J. L. Sonnenberg, D. Williams-Young, F. Ding, F. Lipparini, F. Egidi, J. Goings, B. Peng, A. Petrone, T. Henderson, D. Ranasinghe, V. G. Zakrzewski, J. Gao, N. Rega, G. Zheng, W. Liang, M. Hada, M. Ehara, K. Toyota, R. Fukuda, J. Hasegawa, M. Ishida, T. Nakajima, Y. Honda, O. Kitao, H. Nakai, T. Vreven, K. Throssell, J. A. Montgomery, Jr., J. E. Peralta, F. Ogliaro, M. J. Bearpark, J. J. Heyd, E. N. Brothers, K. N. Kudin, V. N. Staroverov, T. A. Keith, R. Kobayashi, J. Normand, K. Raghavachari, A. P. Rendell, J. C. Burant, S. S. Iyengar, J. Tomasi, M. Cossi, J. M. Millam, M. Klene, C. Adamo, R. Cammi, J. W. Ochterski, R. L. Martin, K. Morokuma, O. Farkas, J. B. Foresman and D. J. Fox, *Gaussian 16, Revision C.01, Gaussian, Inc., Wallingford CT*, 2016.
5. K. Momma and F. Izumi, *J. Appl. Cryst.*, 2011, **44**, 1272-1276.
6. A. Dadlani, S. Acharya, O. Trejo, D. Nordlund, M. Peron, N. Razavi, F. Berto, F. B. Prinz and J. Torgersen, *ACS Appl. Mater. Interfaces*, 2017, **9**, 39105-39109.
7. D. Salusso, E. Borfecchia and S. ordiga, *J. Phys. Chem. C*, 2021, **125**, 22249-22261.